Order-disorder phenomena and octahedral tilting in SrTi$_{1-X}$Sn$_X$O$_3$ perovskites – A structural and spectroscopic study

Anderson B.S. Lavinscky[a], Anna-Maria Welsch[b,c], Brendan J. Kennedy[c,*], Maria I.B. Bernardi[a], Valmor R. Mastelaro[a]

[a] *Physics Institute, University of Sao Paulo, Sao Carlos, SP, Brazil*
[b] *Sydney Analytical Core Facility, University of Sydney, NSW 2006 Australia*
[c] *School of Chemistry, University of Sydney, NSW 2006, Australia*

ARTICLE INFO

ABSTRACT

Oxides of the type SrTi$_{1-x}$Sn$_x$O$_3$ have been prepared using both a solid state and polymeric precursor method and characterized using high-resolution Synchrotron X-ray Diffraction and X-ray Absorption and Raman spectroscopies. The diffraction measurements demonstrate that a continuous pseudo-solid solution exists between the cubic SrTiO$_3$ and orthorhombic SrSnO$_3$ end-members with the same sequence of structures cubic $Pm\bar{3}m$ → tetragonal $I4/mcm$ → orthorhombic $Imma$ → orthorhombic $Pnma$ being observed irrespective of the preparation method. The Raman and XAS measurements revealed the presence of extensive disorder in samples treated at low temperatures, and that this disorder is reduced, but not totally eliminated, by annealing above 1300 °C. It is likely the local structure evolves similarly to that established by S-XRD for samples annealed above 1300 °C. This postulate is supported by the Ti K-edge XANES measurements that showed the local symmetry of the Ti cation evolves systematically as Sn^{4+} ions replace the Ti^{4+} cations in the samples, irrespective of the temperature to which the sample had been heated.

1. Introduction

The large number of studies of materials with the ABO_3 perovskite structure present in the literature reflects the enormous scientific interest in these compounds and the variety of technological applications, such as capacitors [1], microelectronics [2] and gas sensors [3], that rely on perovskites. It is well established that the crystal structure of ABO_3 perovskites is stable to substitutions of both the A and B site cations by ions with different ionic radius and oxidation states, as long as the Goldschmidt tolerance factor is satisfied, allowing a wide range of compositions to be prepared [4,5]. Doped and undoped strontium titanate (SrTiO$_3$) has been the subject of a large number of studies over the years due to its possible applications as a photoluminescent material [6], oxygen gas sensor [7], in dynamic random access memory [8,9], in photocatalysis [10], as a thermoelectric material [11] and in catalysis [12]. Strontium stannate (SrSnO$_3$) has also been widely studied due to its applications in photocatalysis [13], humidity and gas sensors [14,15], solar cells [16] and also, because it exhibits photoactivity for water splitting under UV light irradiation [17]. Some efforts have been dedicated to investigating the effect on the properties of SrTiO$_3$ when Ti^{4+} is substituted by a larger Sn^{4+} ion

forming the SrTi$_{1-x}$Sn$_x$O$_3$ solid-solution [18–27].

The structures of SrTiO$_3$ and SrSnO$_3$ are now well established. At room temperature, SrTiO$_3$ has the simple cubic $Pm\bar{3}m$ perovskite structure. SrSnO$_3$ has a $\sqrt{2}a_p \times \sqrt{2}a_p \times 2a_p$ (where a_p is the equivalent cubic lattice parameter) orthorhombic $Pnma$ structure at room temperature as a consequence of tilting of the corner sharing SnO$_6$ octahedra [28,29]. Despite the presence of such tilts the cell metric of SrSnO$_3$ is, almost perfectly, cubic and establishing the correct space group and symmetry for SrSnO$_3$ required examination of the weak superlattice reflections that arise due to the tilting. There remains considerable uncertainty in the literature regarding the correct structures of the intermediate members of the SrSn$_{1-x}$Ti$_x$O$_3$ solid solution, with different authors proposing different symmetries. Part of this confusion seems to stem from the differing combinations of synthetic and analytical methods employed across the various studies, some of which are summarized below.

Wu et al. synthesized SrSn$_{1-x}$Ti$_x$O$_3$ samples with $x = 0.25$, 0.50 and 0.75 using a solid-state reaction and studied their suitability as humidity sensors [23]. They reported that all the samples formed a single perovskite phase with cubic symmetry after sintering in air at 1250–1400 °C for 2–4 h. The cubic lattice parameter was observed to

---

decrease as the amount of the smaller titanium cation was increased and the best humidity sensing property was seen for SrTi$_{0.5}$Ti$_{0.5}$O$_3$. Xie et al. studied SrSn$_{1-x}$Ti$_x$O$_3$ ceramics with $x = 0$, 0.01, 0.03, 0.05 and 0.07, also prepared by solid-state reaction with the samples heat-treated at 1150 °C for 2 h in air [27]. Using conventional X-ray diffraction measurements, they found single cubic perovskite phase for all compositions studied. They noted that even with such low substitution levels the replacement of Ti^{4+} by Sn^{4+} resulted in a shift of (111) peak toward lower diffraction angles indicative of an increase in the unit cell parameter.

Singh et al. reported studies of the electrical properties of SrSn$_{1-x}$Ti$_x$O$_3$ with $x = 0.10$, 0.20, 0.30, 0.40 and 0.50, where the samples were also prepared by solid-state reaction [24]. They claimed that samples with $0 \leq x \leq 0.40$, sintered at 1500 °C for 12 h, were a single phase with cubic symmetry, but indexed these to a double perovskite unit cell with a ~ 8.0 Å compared to 3.90 Å for SrTiO$_3$. They described the $x = 0.5$ as not being single phase. The single phase samples were semiconductors with modest activation energies ~ 1 eV.

Suzuki *et al.* prepared samples where the Sn ions were added to both the Sr and Ti sites within the range from 0 to 0.1 with $x = a+b$ for Sr$_{1-a}$Sn$_a$Ti$_{1-b}$Sn$_b$O$_3$ (SSTS) compositions and $x = 0.10$ for Sr$_{0.90}$Sn$_{0.10}$TiO$_3$ [18,19]. The samples were prepared by solid-state reaction and sintered at 1300 °C for 2 h in controlled, partial pressure of oxygen, atmosphere. They reported that the SSTS sample with $x = 0.1$ had a cubic structure according to X-ray diffraction measurements [18]. These authors concluded from piezoresponse measurements that the Sn^{2+} ions were preferably located at the off-center position of the Sr^{2+} site [19]. Laurita et al. analyzed the Sr$_{0.9}$Sn$_{0.1}$TiO$_3$ sample prepared by Suzuki et al. [18], by Rietveld refinement of neutron diffraction data, and confirmed this sample to be cubic with space group $Pm\bar{3}m$ [30].

The same group also studied the temperature dependence of the Raman spectra of the Sr$_{1-a}$Sn$_a$Ti$_{1-b}$Sn$_b$O$_3$ ($x = a+b = 0.1$, 0.02 and 0.05) system between 300 and 20 K [26], where the samples were prepared using the same solid state conditions described previously [18]. At 300 K, they observed a peak at ~540 cm^{-1} assigned to the F_{1u} (TO$_4$) mode and another peak at ~120 cm^{-1} assigned to the F_{1u} (TO$_1$) mode, which are not observed in the Raman spectrum of SrTiO$_3$. The intensities of these Raman peaks increased as the amount of Sn was increased and no changes in the frequencies were observed except for the TO$_1$ soft mode (~80 cm^{-1} in $x = 0.02$). They identified a structural phase transition at 150 K by the temperature dependence of the modes at 144 cm^{-1} and 443 cm^{-1}. Recall that SrTiO$_3$ undergoes a structural phase transition to a tetragonal structure in space group $I4/mcm$ near 105 K.

Stanulis et al. used a sol-gel route to prepare SrSn$_{1-x}$Ti$_x$O$_3$ samples with x varying from 0.05 to 0.50 [25]. For compositions $x \leq 0.15$ calcined at 800 °C for 5 h, they obtained a single phase cubic sample. When $x \geq 0.20$, they observed phase separation with the samples being biphasic. These workers reported that increasing of Ti content causes an increase in the intensity of diffraction peaks due to SrTiO$_3$ whereas the intensities of diffraction peaks assigned to SrSnO$_3$ remained essentially constant.

Oliveira et al. investigated the effect of the addition of Ti on the thermal and structural behavior of SrSn$_{1-x}$Ti$_x$O$_3$ for $x = 0.0$, 0.25, 0.50, 0.75 and 1.0 [20]. The powdered crystalline samples were obtained using a polymeric precursor method and were calcined at 700 °C in air for 4 h. These authors reported an orthorhombic $Pbnm$ (an alternate setting of $Pnma$) phase when $x = 0$ and a tetragonal $I4/mcm$ phase for $x = 0.25$. For the other compositions, they found a cubic $Pm\bar{3}m$ phase. These results were confirmed by the presence of vibrational modes around 570 cm^{-1} related to TiO$_3^{2-}$ units, which are typically found in the Raman spectrum of titanium perovskites with cubic symmetry.

As evident from the above brief survey published studies on the SrSn$_{1-x}$Ti$_x$O$_3$ system report a wide variety of results, however, the studies have often only explored limited composition ranges and due to the different methods used to prepare the samples, it is not feasible to

extrapolate from one study to the next. Consequently, only limited information is available about the changes in crystal symmetry across the full series. To fill this gap, SrTi$_{1-x}$Sn$_x$O$_3$ (STSO) ceramic samples with x varying from 0.0 to 1.0 were prepared using both a polymeric precursor method (PPM) and a solid-state reaction method (SSRM). To establish the range of compositions that a single phase solid-solution existed and to determine how the structure evolved as Sn substitutes Ti, the samples were characterized by a high-resolution synchrotron X-ray diffraction (S-XRD), Raman spectroscopy and X-ray absorption near edge structure (XANES) techniques.

2. Experimental

SrTi$_{1-x}$Sn$_x$O$_3$ (STSO) polycrystalline samples with $x = 0.00$, 0.20, 0.40, 0.60, 0.80, 0.85, 0.90, 0.95 and 1.0, were obtained by two different synthesis methods with the samples denoted as STO (SrTiO$_3$), STSO80 (SrTi$_{0.80}$Sn$_{0.20}$O$_3$), STSO60 (SrTi$_{0.60}$Sn$_{0.40}$O$_3$), STSO40 (SrTi$_{0.40}$Sn$_{0.60}$O$_3$), STSO20 (SrTi$_{0.20}$Sn$_{0.80}$O$_3$), STSO15 (SrTi$_{0.15}$Sn$_{0.85}$O$_3$), STSO10 (SrTi$_{0.10}$Sn$_{0.90}$O$_3$), STSO05 (SrTi$_{0.05}$Sn$_{0.95}$O$_3$) and SSO (SrSnO$_3$). The following reagents were used as precursor materials during the synthesis: strontium nitrate (Sr(NO$_3$)$_2$ - Synth, 99%), titanium (IV) isopropoxide (Ti[OCH(CH$_3$)$_2$]$_4$ - Sigma-Aldrich, 99%), Tin Chloride dihydrate (SnCl$_2$· 2H$_2$O − Synth. 98%), Anhydrous Citric Acid (C$_6$H$_8$O$_7$ - Synth 99.5%), Nitric Acid (HNO$_3$ - Synth 65%) Ethylene glycol (C$_2$H$_6$O$_2$ - Synth 99%) and Ammonium Hydroxide (NH4OH - Synth 28%).

2.1. Polymeric precursor method (PPM)

Polymeric resins were synthesized using titanium isopropoxide, Ti[OCH(CH$_3$)$_2$]$_4$, tin chloride dihydrate, SnCl$_2$·2H$_2$O, strontium nitrate, Sr(NO$_3$)$_2$, citric acid, C$_6$H$_8$O$_7$, nitric acid, HNO$_3$, ethylene glycol, C$_2$H$_6$O$_2$, and ammonium hydroxide, NH$_4$OH, as reagents. Titanium citrate and tin citrate were prepared as described in [6,31,32]. Strontium citrate was prepared by dissolving Sr(NO$_3$)$_2$ in a citric acid solution (3:1; citric acid:strontium molar ratio). For each composition, the strontium citrate solution was mixed with the appropriate mixture of titanium citrate, tin citrate and ethylene glycol (40:60; ethylene glycol:citric acid mass ratio) solutions under constant stirring. The temperature was then increased to about 90 °C to obtain the polymeric resins. After pre-treatment of the resin at 300 °C/4 h, a portion of the sample was calcined at 700 °C and 900 °C for 2 h and the remainder was pressed into *pellets* that were sintered for 12 h at 1325 °C and 1350 °C for STO and STSO20, respectively, and at 1400 °C for the remaining compositions. These temperatures were defined according the thermal analysis experiments (not shown) and based in previous studies present in the literature [18–27]

2.2. Solid-state reaction method (SSRM)

Samples were prepared by mixing stoichiometric quantities of strontium carbonate, SrCO$_3$, titanium dioxide, TiO$_2$, and tin dioxide, SnO$_2$, for 24 h in a ball mill with isopropyl alcohol. The mixtures were then dried at 80 °C before being pressed into pellets which were sintered at 1450 °C for 24 h. The sintering temperature was defined according previous studies present in the literature [18–27].

The pellet samples obtained by both methods were powdered and characterized using synchrotron X-ray diffraction at the Brazilian Synchrotron Laboratory (LNLS). X-ray powder diffraction data were collected at the XRD2 beam line over the angular range 5° < 2θ < 120°, using X-rays of 1.033 Å wavelength with the samples housed in 0.5 mm diameter capillaries [33,34].

Raman spectra were collected on a Renishaw InVia Reflex Raman spectrometer under ambient conditions, using the 514 nm laser excitation line, an air-cooled charge-coupled device camera and a 20x Olympus normal objective. An acquisition time of 120 s was employed with two repetitions, in the range from 100 to 1500 cm^{-1}. Raman spectra from each
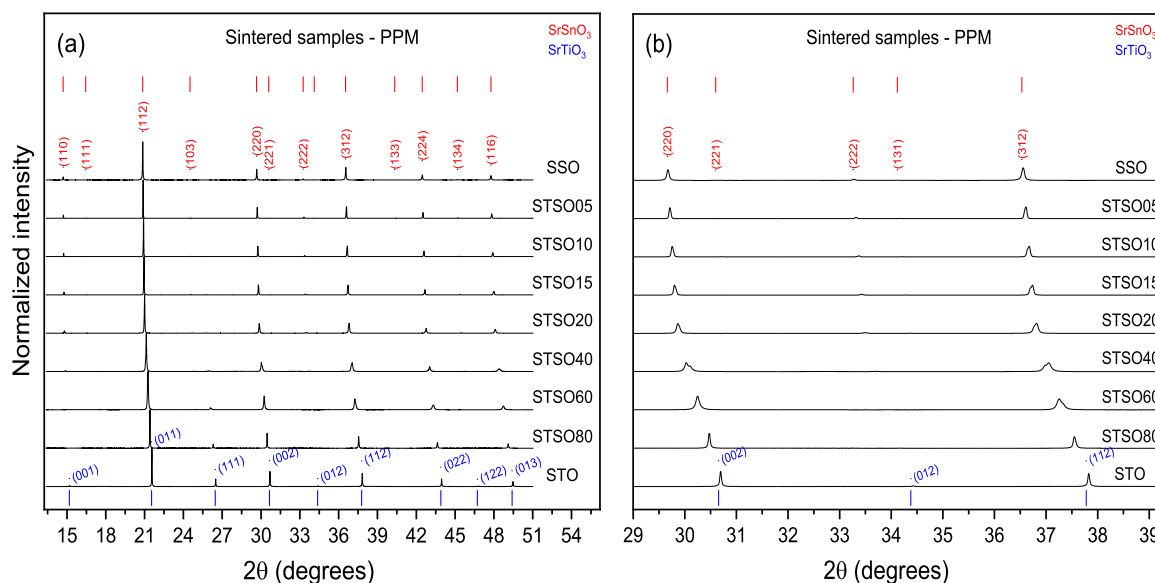
Fig. 1. S-XRD patterns of $SrTi_{1-x}Sn_xO_3$ sintered samples obtained by polymer precursor method (PPM): (a) 2θ range 13–51° and (b) 2θ range 29–39°.

sample were collected from several different positions to verify the uniformity of the samples. None of the spectra exhibited any perovskite-structure related Raman signals above 950 cm^{-1}.

The General Structure Analysis System (GSAS) software package with the EXPGUI front-end was employed for the structural refinements. A pseudo-Voigt peak shape function (GSAS Peak Shape model 4) incorporating the Finger, Cox and Jephcoat asymmetry correction was utilized. The background was estimated using a 15 term shifted Chebyshev function which was refined along with the lattice parameters, profile coefficients, atomic positional parameters and isotropic (U_{iso}) atomic displacement parameters. Refined structural parameters are available in Supplementary material.

X-ray absorption near-edge structure (XANES) spectra were collected at XAFS2 beamline at the LNLS storage ring. Ti K-edge XANES spectra were collected in transmission mode at room temperature in the energy range 4910–5150 eV with 0.3 eV step around the absorption edge. The XANES data were analyzed using the Athena software [35,36].

3. Results and discussions

3.1. X-ray diffraction

Fig. 1 and Supplementary Figs. S1-S2 show S-XRD patterns of the $SrTi_{1-x}Sn_xO_3$ samples prepared using the polymeric precursor method (PPM), but calcined at different temperatures. Fig. 2 shows S-XRD patterns for the same compositions prepared using a solid-state reaction method (SSRM). In all cases, the diffraction patterns show the formation of a perovskite phase irrespective of the thermal treatment temperature.

The diffraction patterns provided no clear evidence for phase separation, although there is noticeable asymmetry in the reflections of the sample with x = 0.6 in Figs. S1 and S2. This asymmetry is not apparent in the sample after it has been heated to 1400 °C for 12 h. The absence of phase separation is consistent with the earlier work of Oliveira et al. but it differs from the report of Stanulis et al. and Singh et al. [20,24,25]. For any given composition, the S-XRD patterns of the STSO-PPM compounds measured at room temperature after heating at 700 °C and 900 °C (Figs. S1 and S2) are very similar, demonstrating an absence of any significant structural change induced by heating to this temperature range. In all cases, the peaks at higher angles are obviously broadened which is indicative of either particle size or strain broadening. This broadening was considerably reduced after heating

the samples to 1400 °C. Irrespective of the heat treatment, the PPM samples showed a systematic shift in peak positions to lower angles as the Ti^{4+} (ionic radii 0.61 Å) was replaced by the larger Sn^{4+} (0.69 Å) cations in the STO lattice (Fig. S1a and S2b). This behavior has been noted in earlier XRD studies of STSO samples [18,20,21,24,25]. As expected, the diffraction peaks for the samples heated to 1400 or 1450 °C (Figs. 1 and 2) were much sharper and systematic changes in the shapes of the high angle peaks were evident, in particular the cubic (211) reflection near 2θ = 38° shows a splitting or reversal of the asymmetry between x = 0.4 and 0.6.

The tendency for the STSO perovskites to have symmetry lower than cubic can be estimated by consideration of the Goldschmidt tolerance factor [37,38]. In our case, as the Sn^{4+} ions are expected to occupy the octahedral B site, the equation becomes:

$$t = \frac{r_{Sr}^{2+} + r_O^{2-}}{\sqrt{2}\left[(1-x)r_{Ti}^{4+} + xr_{Sn}^{4+} + r_O^{2-}\right]} \tag{1}$$

where the ionic radii for the appropriate coordination environment of Ti^{4+}, Sn^{4+}, O^{2-} and Sr^{2+} are taken from Shannon's table of ionic radii [39]. The calculated tolerance factor (t) values decrease as the Sn content increases and lie in the range 0.96–1.00, well within the range appropriate for the perovskite structure, i.e., 0.71 < t < 1.05. The reduction in t, as the Sn content is increased, favors the presence of cooperative tilting of the corner sharing octahedra and consequent lowering of symmetry.

To quantitatively interpret the trends observed in the XRD patterns of the sintered samples, Rietveld refinements were undertaken using high-resolution synchrotron X-ray diffraction (S-XRD) data. Before doing this, the patterns were examined for the presence of weak superlattice reflections indicative of cooperative tilting of the octahedra. The presence of in-phase (+) and out-of-phase (−) tilts of the octahedra could be identified through the presence of two-odd one-even (ooe) integer and all-odd (ooo) integer superlattice reflections, respectively. The former is associated with softening at the R-point (k = ½ ½ ½) of the Brillioun zone and the latter with softening at the M-point (k = ½ ½ 0). The high signal-to-noise statistics of the present synchrotron diffraction data allows us to unequivocally establish the nature of the tilting of the octahedra and cell symmetry. Table 1 shows the space groups, symmetry and lattice parameters obtained from the refinement against the S-XRD patterns of the STSO sintered samples obtained by both synthesis methods, and these are in good agreement with data present in the literature for the end-members samples
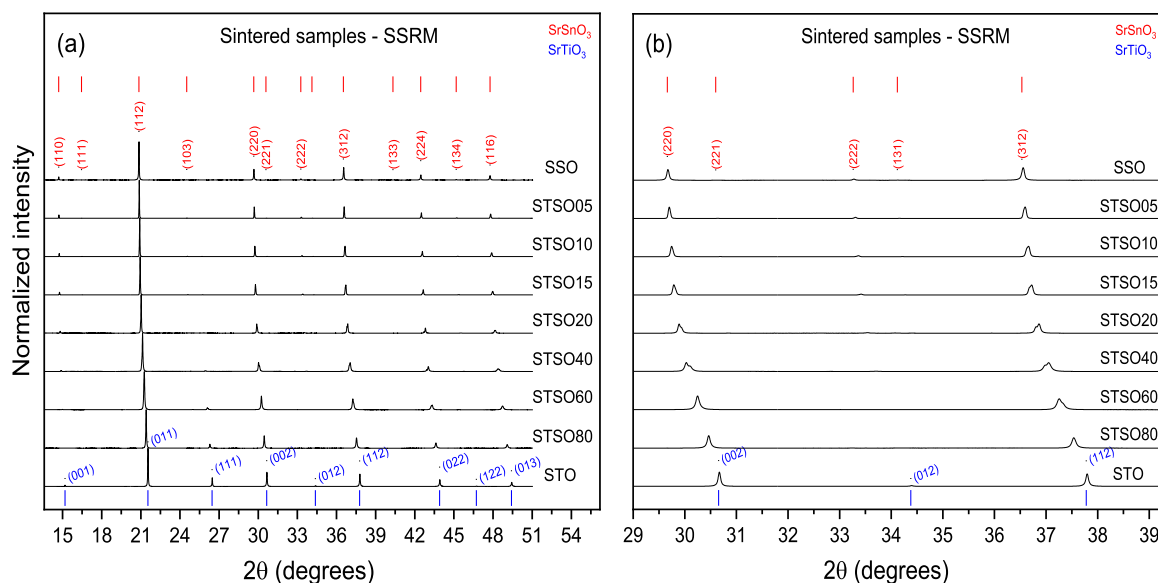
Fig. 2. S-XRD patterns of the STSO samples obtained by solid-state reaction method (SSRM) sintered at 1450 °C/24 h, for (a) 2θ range 13–51° and (b) 2θ range 29–39°.

($SrTiO_3$ and $SrSnO_3$) [20,28].

Considering firstly the samples prepared by the solid-state reaction method (SSRM), a cubic $Pm\bar{3}m$ model with a = 3.90177(2) Å fits well the S-XRD data of the undoped STO sample. The S-XRD data of the STSO80 sample shows the presence of a very weak reflection at 25

degrees, indicating the presence of out-of-phase tilting of the octahedra and that, therefore, the structure is not cubic. Initially, it was attempted to fit the data using a single phase tetragonal $I4/mcm$ model, this being observed in $SrTiO_3$ below 105 K as well as in Ca-doped $SrTiO_3$ [40]. This, however, did not account for the asymmetry/splitting of a small

Table 1

Refinement by Rietveld of Synchrotron XRD data of the sintered samples obtained by solid-state reaction (SSRM) and polymer precursors (PPM) methods. The data for the two series (Solid State and Polymer precursor) were measured at different times. Where the *Imma* and *I4/mcm* phases co-exist the weight percentage of each phase is given. Further details are availbe in Supplementary material.

Sample	Solid state reaction			Polymer precursor		
	Symmetry+Space group	Lattice parameters (Å)		Symmetry+Space group	Lattice parameters (Å)	
STO	cubic $Pm\bar{3}m$	a = 3.91001(1)	V_{cell} = 59.777(1)	cubic $Pm\bar{3}m$	a = 3.90177(2)	V_{cell} = 59.400(1)
STSO80	orthorhombic *Imma* 56.4(2) wt %	a = 5.56484(8) b= 5.5722(1) c= 7.8736(2)	V_{cell} = 244.146(5)	tetragonal *I4/mcm*	a = 5.5568(2) c = 7.8604(4)	V_{cell} = 242.714(4)
	tetragonal *I4/mcm* 43.6(2) wt %	a = 5.5703(5) c = 7.8748(14)	V_{cell} = 244.347(6)			
STSO60	orthorhombic *Imma* 58.9(7) wt %	a = 5.61478(9) b = 5.59604(8) c = 7.9213(1)	V_{cell} = 248.892(9)	orthorhombic *Imma* 56.8(2) wt %	a = 5.60286(9) b = 5.5842 2(8) c = 7.90436(13)	V_{cell} = 247.31(1)
	tetragonal *I4/mcm* 41.1(9) wt %	a = 5.60772(9) c = 7.9347(2)	V_{cell} = 249.520(9)	tetragonal *I4/mcm* 43.2(2) wt %	a= 5.59555(9) c = 7.9185(1)	V_{cell} = 247.93(1)
STSO40	orthorhombic *Imma*	a = 5.65575(4) b = 5.63901(4) c = 7.96770(6)	V_{cell} = 254.112(5)	orthorhombic *Imma*	a = 5.64382(5) b = 5.62710(4) c = 7.95087(6)	V_{cell} = 252.506(6)
STSO20	orthorhombic *Pnma*	a = 5.68630(5) b = 5.67432(5) c = 8.02329(6)	V_{cell} = 258.879(5)	orthorhombic *Pnma*	a = 5.67432(4) b = 5.66238(5) c = 8.00642(6)	V_{cell} = 257.248(5)
STSO15	orthorhombic *Pnma*	a = 5.68875(2) b = 5.67731(2) c = 8.02734(3)	V_{cell} = 259.260(2)	orthorhombic *Pnma*	a = 5.68565(1) b = 5.67492(1) c = 8.02473(2)	V_{cell} = 258.923(1)
STSO10	orthorhombic *Pnma*	a = 5.69609(2) b = 5.6865(2) c = 8.04053(3)	V_{cell} = 260.423(2)	orthorhombic *Pnma*	a = 5.69333(1) b = 5.68431(1) c = 8.03833(2)	V_{cell} = 260.142(1)
STSO05	orthorhombic *Pnma*	a = 5.70338(2) b = 5.695987(2) c = 8.05442(2)	V_{cell} = 261.654(2)	orthorhombic *Pnma*	a = 5.70067(9) b = 5.69375(1) c = 8.05164(1)	V_{cell} = 261.342(1)
SSO	orthorhombic *Pnma*	a = 5.71069(6) b = 5.69931(6) c = 8.05930(8)	V_{cell} = 262.306(7)	orthorhombic *Pnma*	a = 5.69918(3) b = 5.68756(3) c = 8.04257(4)	V_{cell} = 260.695(2)

number of reflections such as the $(222)_p$ near 54 degrees, here the index refers to the primitive cubic cell. The *I4/mcm* tetragonal structure forms as a result of out-of-phase tilts about the *c*-axis ($a^0a^0c^-$ in Glazer's notation). To fit the S-XRD pattern, a two-phase tetragonal *I4/mcm* + *Imma* model was used. The orthorhombic *Imma* model also only contains out-of-phase-phase tilts, but in this case, they are about the [110] axis, (tilt system $a^-a^-c^0$). Howard and Stokes [41] have shown that an *I4/mcm* to *Imma* transition must be first order since it involves a reorientation of the tilting from [110] to [001], and co-existence of these two phases has been observed in some perovskite systems, including $Ba_{1-x}Sr_xSnO_3$ and $Ba_{1-x}Sr_xHfO_3$ [29,42]. The S-XRD data for STSO60 also only displayed superlattice reflections, associated with the out-of-phase tilting of the BO_6 octahedra, and there is no evidence for the presence of in-phase tilting. The $(222)p$ reflection near 54 degrees is clearly split and modeling this required the same two-phase, *Imma* and *I4/mcm* model used for the STSO80 sample. Phase separation can occur for a number of reasons, including, defects or sample inhomogeneities, or it may be a consequence of kinetics of the transformation. In the present case, it is postulated that defects form, possibly by local clustering of the Ti or Sn into Sn-rich and Ti-rich nanodomains, which act to trap the higher *I4/mcm* symmetry structure upon cooling from the synthesis temperature. The Raman spectra described below provide evidence for the disorder.

The only superlattice reflections observed in the S-XRD pattern of STSO40 were indicative of out-of-phase tilts of the octahedra and, together with the splitting of the stronger Bragg reflections suggested this was orthorhombic in *Imma* space group. Such a model well reproduces the data. The S-XRD profiles of the remaining 5 samples displayed superlattice reflections indicative of the presence of both in-phase and out-of-phase tilting of the octahedra suggesting that the orthorhombic space group *Pnma* observed for undoped $SrSnO_3$ was appropriate. Rietveld refinements confirmed this, and the data for the five samples (STSO20, STS015, STSO10, STSO05, and SSO) were well fitted by a *Pnma* orthorhombic model.

The Rietveld refinement of S-XRD data of sintered polymer precursor method samples yielded very similar results to those obtained for the samples prepared by the solid-state reaction method. The one exception was the STSO80 sample for which a satisfactory fit was obtained using a single phase *I4/mcm* model. For the STSO60 sample, the S-XRD data were consistent with the same two-phase k, orthorhombic − tetragonal (*Imma - I4/mcm*) model described above. Superlattice reflections, associated with the in-phase tilting of the BO_6 octahedra, were not observed in the S-XRD pattern of STSO40 and space group *Imma* appeared to be appropriate. The data from SSO, STSO05, STSO10, STSO15 and STSO20 samples were well fitted to a *Pnma* model and for each of these the S-XRD patterns contained superlattice reflections consistent with the presence of both in-phase and out-of-phase tilts.

Fig. 3 shows two examples of the Rietveld refinement for the STSO80 sample. The sample prepared using the solid-state method (Fig. 3a) was refined using an orthorhombic *Imma* and tetragonal *I4/mcm* models, whereas the XRD data of the sample obtained from the polymeric precursor method (Fig. 3b) was fitted with only a tetragonal *I4/mcm* model.

The composition-dependent evolution of the unit cell volume of the $SrTi_{1-x}Sn_xO_3$ system prepared using solid-state and polymeric precursor methods, with its respective space group, are summarized in Fig. 4.

3.2. Raman spectroscopy

Raman data for each series are presented in Figs. 5 and 6. Spectra were temperature and baseline corrected and the intensities have been scaled for ease of comparison. The Raman spectrum collected for STSO20, obtained by polymer precursor method and calcined at 700 °C/2 h, showed a structure that was inconsistent with perovskite, and displayed peaks at odd with the rest of the series, indicating that
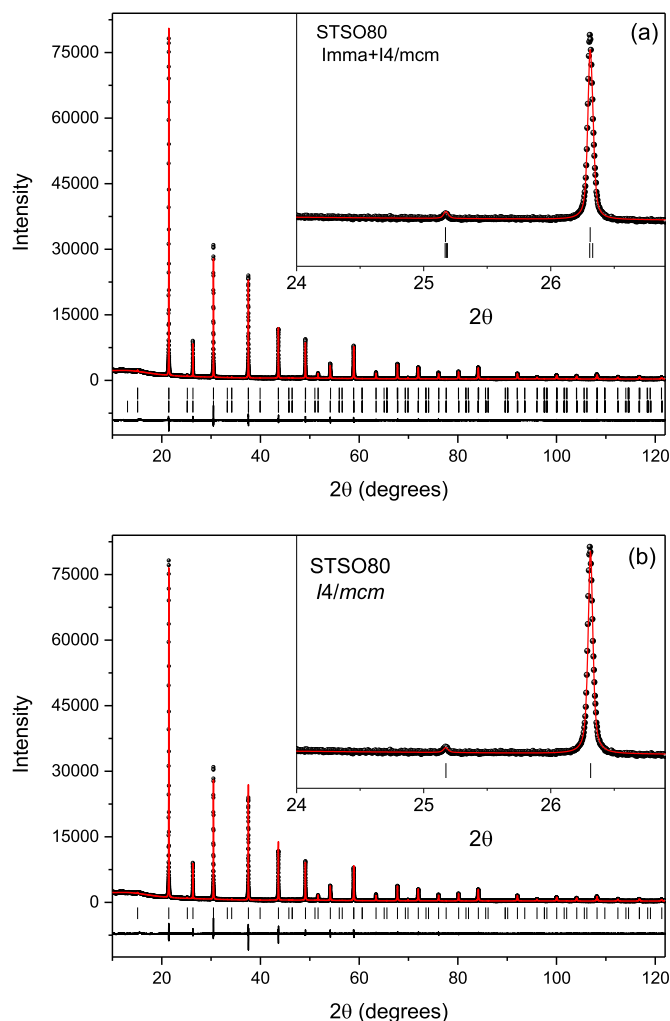

Fig. 3. Rietveld refinements of STSO80 sample obtained by (a) solid-state reaction (SSR) and by (b) polymer precursor (PP) methods.
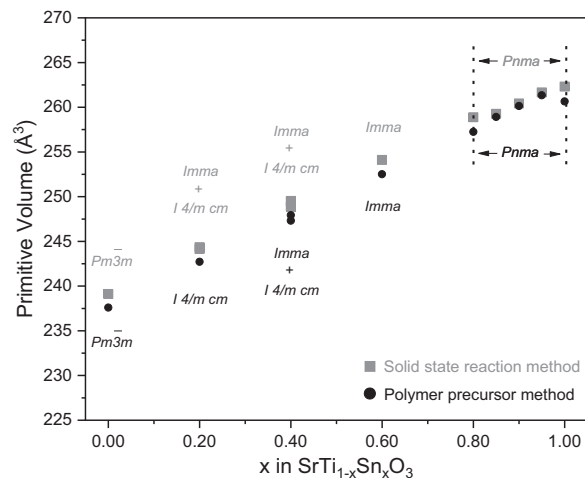

Fig. 4. Structure-dependency variation of the unit-cell volume of STSO samples. The value for the cubic cell of STO (x = 0.00) was multiplied by 4 to allow the comparison of the data of all samples.

the sample has not totally reacted through to the desired product. For this reason, it was omitted from the series. Additionally, the Raman spectra of the samples prepared using the polymeric precursor method at lower temperatures, i.e. 700 and 900 °C, reveal peaks belonging to strontianite, $SrCO_3$, at ca. 150, 185, 690 and 1075 cm^{-1}, marked with
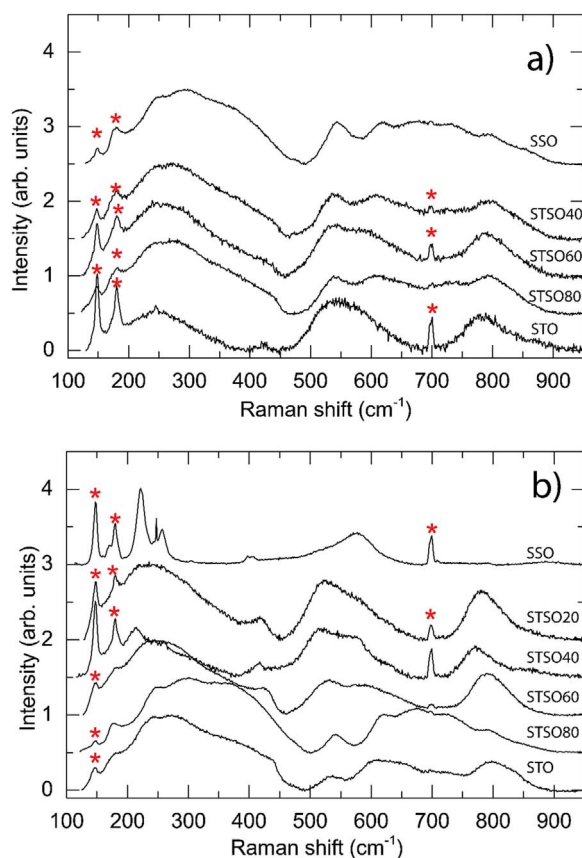
Fig. 5. Raman spectra of samples prepared by the polymeric precursor method: a) calcined at 700 °C and b) calcined at 900 °C. Red stars mark the peaks from strontianite, SrCO₃. The spectrum collected for STSO20, prepared by the polymer precursor method and calcined at 700 °C/2 h, was inconsistent with perovskite, and for this reason, it was omitted from the series.

Fig. 6. Raman spectra of samples prepared by a) solid-solution reaction sintered at 1450 °C and b) by polymer precursor method, sintered above 1300 °C.

red stars in Fig. 5. Stanulis et al. [25] have previously reported the presence of $SrCO_3$ in samples only heated to low temperatures. The presence of $SrCO_3$ phase is not evident in the spectra of samples heated above 900 °C suggesting it is derived from incomplete reaction rather than as a consequence of exposure of the sample to atmospheric CO_2. No signature of strontianite was observed in the Raman spectra for samples after they had been sintered at 1400 °C, nor in the spectra of samples prepared using the solid-state reaction method sintered at 1450 °C.

To quantify the observed spectral changes, the spectra were curve-fitted using Lorentzian profiles. Given the different number of Lorentzians necessary to fit the spectra for the end members in each solid solution series, the curve-fitting strategy involved starting from the STO side and developing the parameters to the SSO end, as well as starting at the SSO end and driving the fit to the STO end. To confirm the results, the match of the fit and the number of required replicas, random blind fits were performed for individual mixed members without reference to the established evolution of parameters. This strategy, whilst time-consuming, resulted in satisfactory matches between the experimental and calculated curves, where the average reduced χ^2 values are in the order of magnitude 10^{-5} and R-square is of the order of 0.999. Figs. 7 and 8 show the evolution of the relevant parameters of the B-cation related modes, namely the individual peak shifts and summed intensities. Intensity values are given as calculated normalized intensities, where individual intensities are scaled by the sum of all peak intensities for each spectrum. In this way it is easier to contextualize the evolution of the intensities of individual peaks regarding the structural transformation with increasing Sn-content. Summed normalized intensities, presented in Figs. 7 and 8, emphasize
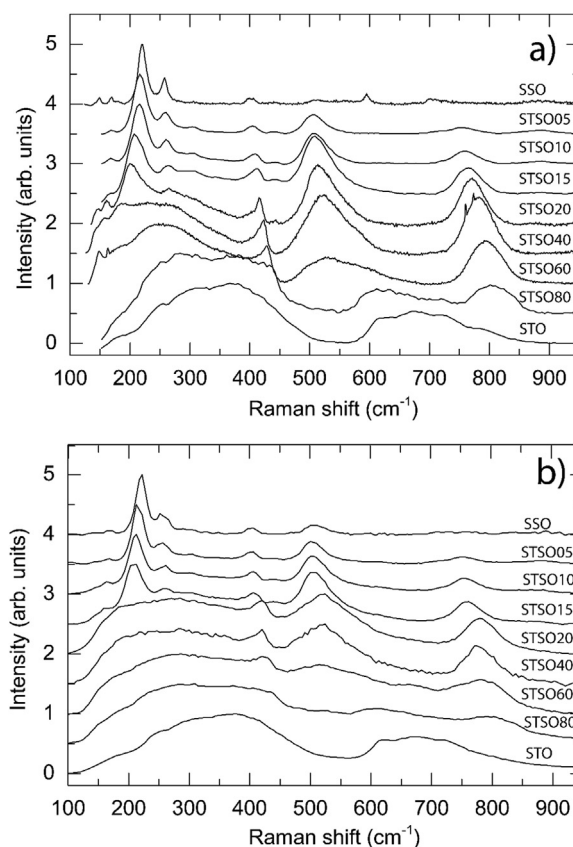
the evolution of the peaks with the change in chemistry most notably in the regions between 200 and 300, 300 and 400, 500 and 650 and 700–850 cm⁻¹.

From the Raman spectra, it is evident that the addition of the Sn-cation induces considerable changes to the, initially simple, perovskite structure of STO. In samples prepared via the polymeric precursor method and calcined at or below 900 °C, the presence of a carbonate phase ($SrCO_3$) is evidence that the reaction is not as initially envisaged, and consequently that the chemistry of the main perovskite phase is not as designed, given that the carbonate sequests a considerable amount of the Sr. It is possible that in this case the Sn cations partially occupy the A-site as described by Suzuki et al. [18]. Additionally, the quality of the spectra, i.e., signal-to-noise, is quite poor for the Ti-rich side of the polymeric precursor synthesized samples, calcined at 700 and 900 °C. This is believed to reflect a low degree of crystalline order since poor signal-to-noise in Raman spectra often occurs in materials with very disordered crystallites. Higher calcination temperatures gave samples that yielded Raman spectra with good signal-to-noise signals indicating that this, at least partially, reduced the disorder. Given the disorder and that the presence of carbonate is an indication of phase inhomogeneity, we shall focus on Raman results collected for samples heated-treated above 1300 °C.

The crystallographic symmetry of the STO end member is primitive cubic in space group $Pm\bar{3}m$, based on the S-XRD results. The normal optical phonon modes predicted by group theory for this structure are $3F_{1u} + F_{2u}$, where F_{1u} is IR-active, and F_{2u} is optically inactive [43]. None of the modes are, in a perfectly ordered $Pm\bar{3}m$ structure, Raman-active. The region between about 200 and 500 cm⁻¹ would be predominantly marked by various vibrations involving B-cation, A-cation and bending of bonds with oxygen [44]. The range between 600 to ca. 800 cm⁻¹ would be marked by stretching vibrations of the BO_6 octahedra in local diagonal [111] distortion of the cubic symmetry.
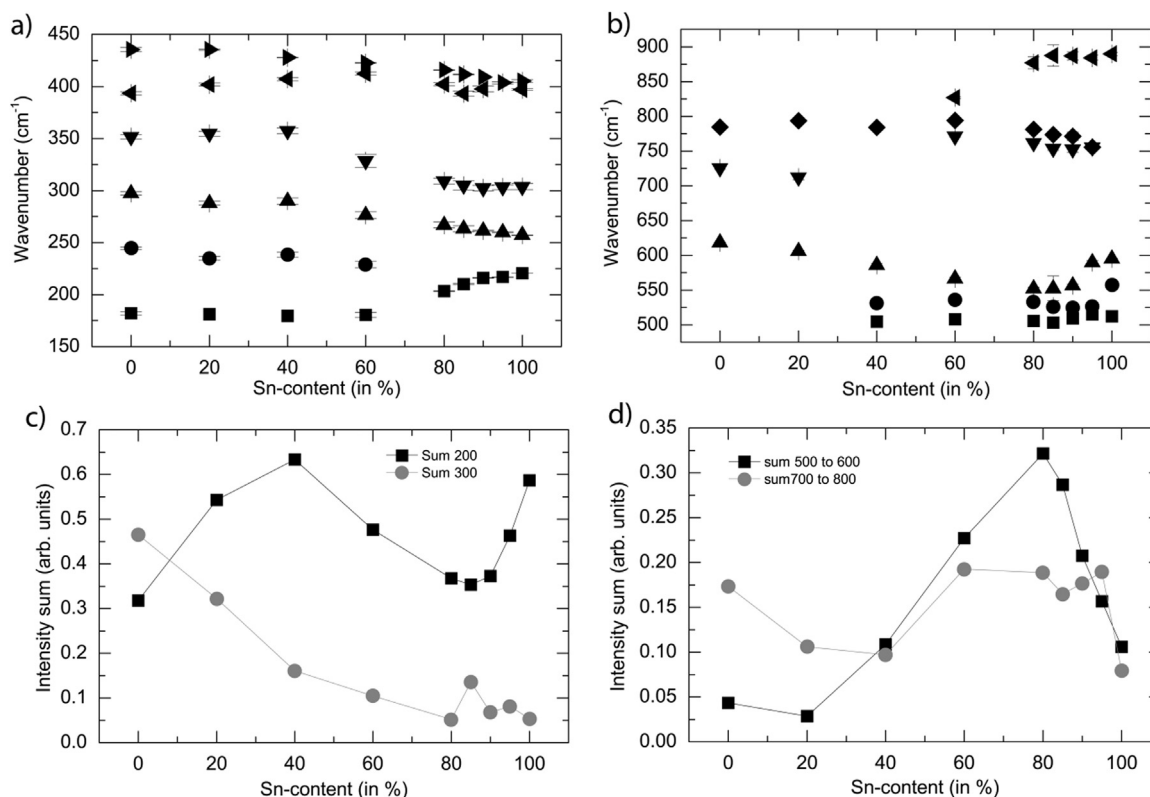
Fig. 7. Evolution of the Raman curve-fitting parameters for solid-solution reaction sample series calcinated at 1450 °C: a) Raman peak shift for modes between 150 and 450 cm^{-1}, involving vibrations in B-cation sublattice and coupled *A*-site and *B*-site cations; b) Raman peak shift for modes between 500 and 900 cm^{-1}, including BO_6 octahedral bending and stretching modes; c) Sum of normalized intensities grouped between 200 and 300 cm^{-1}, involving vibrations between *A*- and *B*-sublattice and 300 and 400 cm^{-1} involving predominantly *B*-O modes and d) Sum of normalized intensities in the high wavenumber envelope showing drop of intensities and disappearance of BO_6 bending (ca. 500–600 cm^{-1}) and stretching modes (ca 600–800 cm^{-1}). The change in symmetry induces a change in a number of modes in the high wavenumber envelope.

That broad bands are present in the Raman spectra of STO indicates that, even after heating to above 1300 °C, there is disorder in the *B*-sublattice. Given the broadness of the observed bands, it is very difficult to determine, with certainty, individual contributing modes and in that respect, the STO end members produced by solid-state and polymer precursor methods give very similar Raman spectrum.

If we consider the SSO end member, the orthorhombic *Pnma* symmetry allows 24 Raman active modes, i.e., $7A_g + 5B_{1g} + 7B_{2g} + 5B_{3g}$. The two strongest peaks, near 223 and 259 cm^{-1}, are both relatively sharp and have been assigned to A_g modes involving Sn-O bending movement along and perpendicular to *c*-axis, respectively [45]. The addition of Ti results in broadening of these peaks, as well as the more obvious growth of broad peaks near 500 cm^{-1}, see Fig. 6, indicative of some degree of local disorder due to the mixed occupancy of the Sn and Ti at the center of the BO_6 octahedra.

The S-XRD results confirm that the addition of Sn to the lattice results in an increase in the unit cell volume and a reduction in symmetry. Regarding the vibrational modes, it reasonable to postulate that the B-cation related modes would be most impacted by the presence of two cations with different masses and effective radii, whereas the modes derived from the *A*-site cation will not be as significantly impacted. This positional disorder will complicate the appearance of the Raman spectra and may mask changes due to lowering of the long-range symmetry. Nevertheless, the spectral changes illustrated in Fig. 6 suggest that there are intermediate structural phases between the Ti and Sn end members in samples synthesized using either the solid-state or polymer precursor methods. For both series, the spectra of STO is dominated by broad features near 350 and 650 cm^{-1} and Sn doping results in a new feature near 800 cm^{-1} that shifts to lower frequency as the Sn content increases. The Raman spectra suggest that there may be at least two intermediate

phases, between 80% and 40% Ti and 20–5% Ti in the solid-state samples and between 80% and 20% Ti and between 15% and 5% Ti for the polymer precursor products. This is similar but not identical to the transitions observed in the S-XRD analysis which shows the presence of four distinct phases. The lack of a simple, direct correlation between the S-XRD and Raman results reflect the length scales of the two measurements, the former probes the long-range or average structure while the latter is sensitive to local disorder. For example, broadening of Raman lines is visible in the polymer precursor series up to 60% Ti (Fig. 6b) and it does not seem feasible to identify a region where the tetragonal *I4/mcm* phase is present. Similarly, the Raman spectra from the samples prepared by the solid-state reaction are suggestive of local ordering at the *B*-sublattice when the Ti content is below 80% (Fig. 6a). In tin-rich samples, with Ti content below 20%, the appearance of additional modes between 200 and 250, 300 and 400, 500 and 600 and 750–800 cm^{-1} is indicative of a change in symmetry.

That the evolution of the spectral signatures for the samples differs between the two series is an indication that the local ordering of the Sn and Ti cations is extremely sensitive to the exact synthesis conditions. The increase in the Sn-content drives spatial ordering in the *B*-sublattice and affects the modes involving the *A*-site cation. The inclusion of the larger Sn-cation also introduces deformation of the unit cell into the orthorhombic symmetry, as observed by S-XRD. Parameters derived from the spectral fitting are presented in Figs. 7 and 8, where they are grouped in lower and higher wavenumber areas, relative to the predominating modes. The changes in these figures indicate that the transformation into orthorhombic symmetry decouples spatially related modes, such as the translational vibrations between the *B*-site and *A*-site cations via oxygen bridges or octahedral torsion, which would occur as a consequence of different types of *B*-cations. It appears that in the SSO end members with 100% Sn-content, modes involving *B*-cations vs.
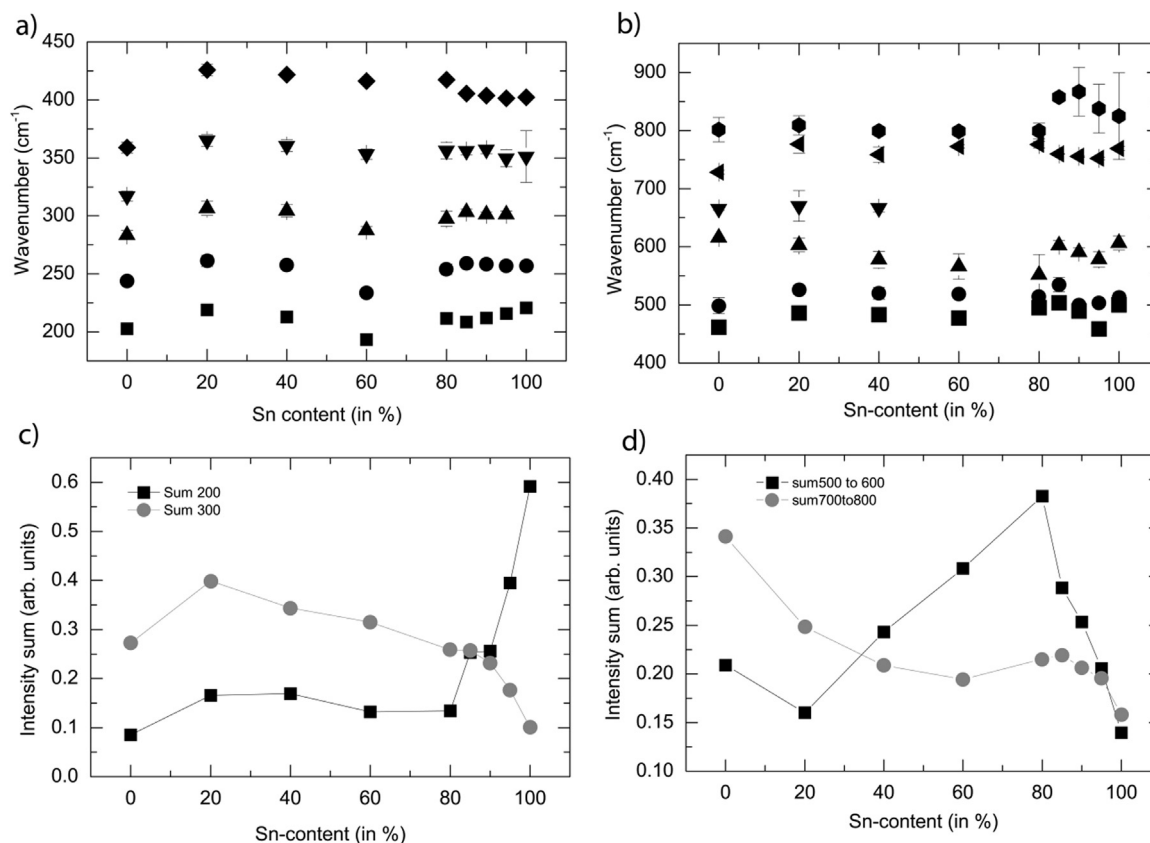
Fig. 8. Evolution of the Raman curve-fitting parameters for polymer precursor reaction sample series calcinated above 1300 °C: a) Positions of the low wavenumber modes between 150 and 450 cm^{-1}, involving vibrations in B-cation sublattice and coupled *A*-site and *B*-site cations; b) Positions of the high wavenumber modes between 500 and 900 cm^{-1}, including BO_6 octahedral bending and stretching modes; c) Sum of normalized intensities between 200 and 300 cm^{-1}, involving vibrations between *A*- and *B*-sublattice and 300 and 400 cm^{-1} involving predominantly *B*-O modes and d) Sum of normalized intensities in the high wavenumber envelope showing drop of intensities and disappearance of BO_6 bending (ca. 500–600 cm^{-1}) and stretching modes (ca. 600–800 cm^{-1}). The change in symmetry induces a change in some modes in the high wavenumber envelope. Evolution of mode parameters across the chemical range differs from the values obtained for solid-solution series.

surrounding oxygen cage are Raman inactive.

3.3. XANES spectroscopy

The Ti K-edge XANES spectra of STSO samples obtained from the polymeric precursor method (PPM) calcined at 700 °C and 900 °C and sintered at temperatures ranging 1325–1400 °C are presented in

Figs. 9–12. The Ti K-edge XANES spectra of STSO solid-state reaction method (SSRM) samples sintered at 1450 °C are presented in Fig. 12. The XANES spectra of all the samples show the presence of three pre-edge peaks characteristic of crystalline SrTiO$_3$ [32,46,47]. According to the literature, peak *A* corresponds to the *1s-3d* (e_g) quadrupolar transition in the titanium atoms whereas peak *B* has both a quadrupolar *1s-3d* (t_{2g}) component and a dipolar one to a *p*-like state
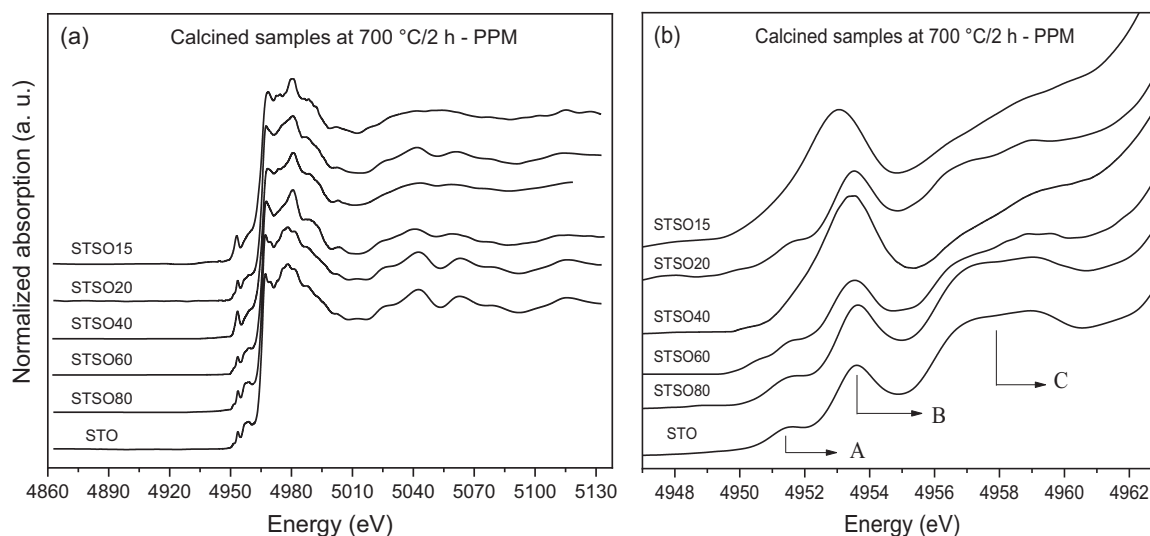

Fig. 9. (a) XANES spectra at the Ti K-edge of PPM - STSO samples calcined at 700 °C/2 h obtained by the polymeric precursor method (PPM); (b) XANES pre-edge region.
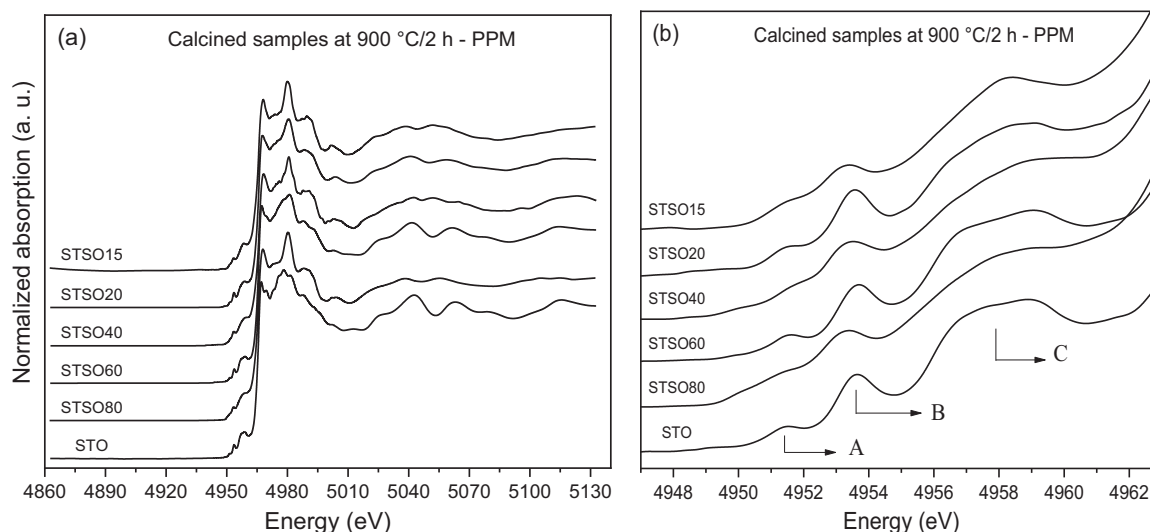
Fig. 10. (a) XANES spectra at the Ti K-edge of STSO samples calcined at 900 °C/2 h obtained by the polymeric precursor method (PPM); (b) XANES pre-edge region.

induced by the hybridization of the *3d* states with the *p* states of the surrounding oxygen [47]. Peak *C* is due to the neighboring of titanium atoms and has a dipolar character. According to the literature, in perovskites, the area of peak *B* is proportional to the average displacement of the Ti atom about its centrosymmetric position in the TiO_6 octahedra [48,49].

Analysis of the XANES spectra shows that the substitution of Ti^{4+} by Sn^{4+} causes significant changes in the pre-edge transitions as well as in the post-edge region. The edge position is, however, invariant of the Sn^{4+} concentration and is indicative of tetravalent Ti. The substitution of the Ti^{4+} ion by the Sn^{4+} ion at the *B* site in the ABO_3 perovskite structure does not require charge compensation. There is, however, a difference between the ionic radii of Ti^{4+} and Sn^{4+} which promotes a change in the local and long-range order structure.

For the samples calcined at 700 °C (Fig. 9), the increasing of intensity of pre-edge peak *B* can be interpreted as an increase in the local disorder around the Ti atoms as the amount of Sn increases. The increase in the intensity of peak *B* as Sn is added can be related to the tilting of the Ti octahedron, observed in S-XRD data. The smoothing of the oscillations after the edge as the amount of Sn increases is indicative of increased disorder around the Ti atoms. Different behavior was observed between the samples calcined at 900 °C and for the sintered samples (Figs. 10–

12), with a significant decrease in the intensity of peak *B* indicating a decrease in the disorder around the Ti atoms. The increase in Sn content also causes a significant modification in the peak *C*, which is related to structural changes in the region of Ti neighboring atoms induced by the substitution of Ti^{4+} by Sn^{2+}.

4. Conclusion

Oxides of the type $SrTi_{1-x}Sn_xO_3$ have been prepared using both a solid state and polymeric precursor method and characterized using high-resolution S-XRD and XAFS and Raman spectroscopies to establish the symmetry and structures present so to resolve the conflicts that exist in the literature regarding these. S-XRD measurements demonstrate that a continuous pseudo-solid solution exists between cubic $SrTiO_3$ and orthorhombic $SrSnO_3$ with the sequence of structures cubic $Pm\bar{3}m$ → tetragonal $I4/mcm$ → orthorhombic $Imma$ → orthorhombic $Pnma$ being observed in samples prepared using either SSM or PPM synthetic methods. Establishing this sequence required high-resolution powder diffraction data to detect and model the subtle peak broadening/splitting and excellent counting statistics to detect the presence of superlattice reflections at arise due to the cooperative rotations of the corner sharing octahedra. The S-XRD measurements demonstrate
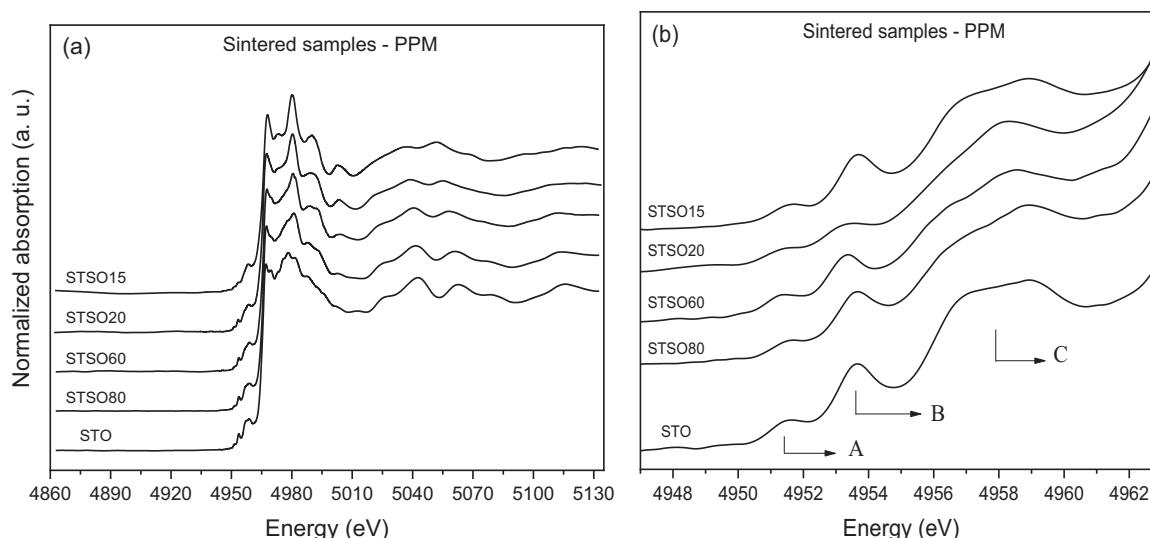

Fig. 11. (a) XANES spectra at the Ti K-edge of STSO sintered samples obtained by polymeric precursor method (PPM); (b) XANES pre-edge region.
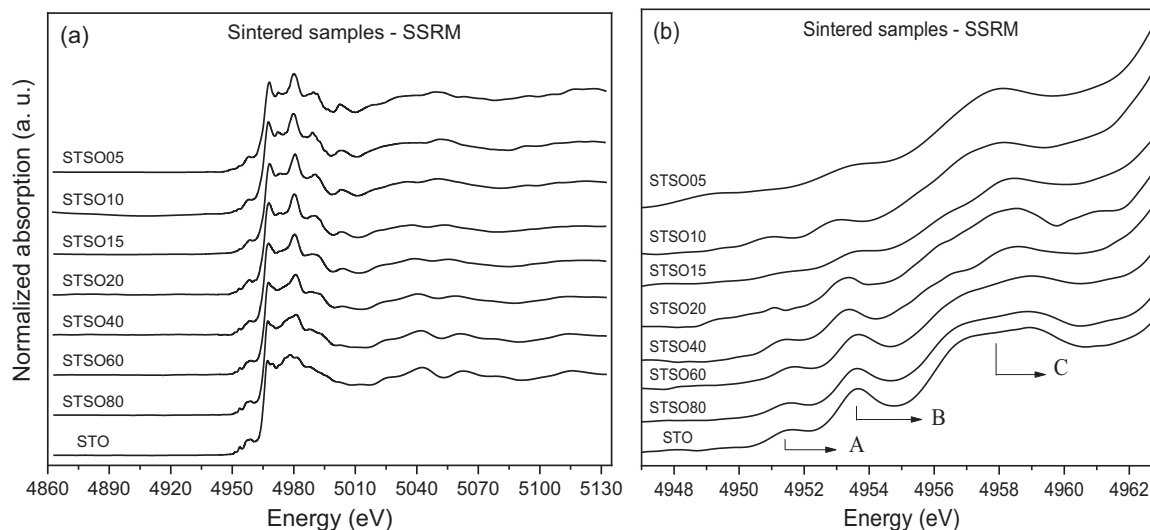
Fig. 12. XANES spectra at the Ti K-edge of (a) STSO sintered samples obtained by solid-state reaction method (SSRM); (b) pre-edge region zoom.

that the long-range (average) structures of the $SrTi_{1-x}Sn_xO_3$ samples are not significantly impacted by the method (SSM vs PPM) used to prepare them, although small differences in phase composition around the two-phase (*Imma-I4/mcm*) region are apparent. We postulate that many of the inconsistencies in the existing literature reflect the use of lower resolution and/or poor counting statistics diffraction data.

It was not feasible to unequivocally establish the symmetry or precise structures for samples prepared using the PPM if the samples were only heated to modest temperatures (700 or 900 °C) due to the broadening of the diffraction peaks. The Raman spectra did, however, provide evidence for structural transitions across the series. The Raman spectra of the non-annealed samples revealed the presence of extensive disorder in samples treated at low temperatures, and that this disorder is reduced, but not totally eliminated by annealing above 1300 °C. Nevertheless, since the space group symmetry reflects the relative effective size of the cations on the perovskite *A* and *B* cation sites as quantified by the tolerance factor it is likely the local structure evolves similarly to that established for the annealed samples. This postulate is supported by the Ti K-edge XANES measurements that showed the local symmetry of the Ti cation evolves systematically as Sn^{4+} ions replace the Ti^{4+} cations in the samples, irrespective of the temperature to which the sample had been heated.

Acknowledgment

Appendix A. Supporting information

Supplementary data associated with this article can be found in the online version at doi:10.1016/j.jssc.2018.10.006.

References

[1] X.Y. Wei, X. Yao, Preparation, structure and dielectric property of barium stannate titanate ceramics, Mat. Sci. Eng. B-Solid 137 (1–3) (2007) 184–188.

[2] A.-M. Azad, T.Y. Pang, M.A. Alim, Ultra-low temperature coefficient of capacitance (Tcc) of the SrSnO3-based electrical components, Act. Passiv. Electron. Compon. 26 (3) (2003) 151–166.

[3] C. Tragut, K.H. Hardtl, Kinetic-behavior of resistive oxygen sensors, Sens. Actuators B-Chem. 4 (3–4) (1991) 425–429.

[4] H.D. Megaw, Crystal structure of double oxides of the perovskite type, Proc. Phys. Soc. Lond. 58 (326) (1946) 133.

[5] G.A. Samara, The relaxational properties of compositionally disordered ABO3 perovskites, J. Phys.-Condens Matter 15 (9) (2003) R367–R411.

[6] L.F. da Silva, L.J.Q. Maia, M.I.B. Bernardi, J.A. Andres, V.R. Mastelaro, An improved method for preparation of SrTiO3 nanoparticles, Mater. Chem. Phys. 125 (1–2) (2011) 168–173.

[7] T. Hara, T. Ishiguro, N. Wakiya, K. Shinozaki, Oxygen sensitivity of perovskite-type dielectric thin films, Mater. Sci. Eng. B-Adv. 161 (1–3) (2009) 142–145.

[8] A.A. Sirenko, C. Bernhard, A. Golnik, A.M. Clark, J.H. Hao, W.D. Si, X.X. Xi, Soft-mode hardening in SrTiO3 thin films, Nature 404 (6776) (2000) 373–376.

[9] P.C. Joshi, S.B. Krupanidhi, Structural and electrical characteristics of SrTiO3 thin-films for dynamic random-access memory applications, J. Appl. Phys. 73 (11) (1993) 7627–7634.

[10] R. Konta, T. Ishii, H. Kato, A. Kudo, Photocatalytic activities of noble metal ion doped SrTiO3 under visible light irradiation, J. Phys. Chem. B 108 (26) (2004) 8992–8995.

[11] T. Okuda, K. Nakanishi, S. Miyasaka, Y. Tokura, Large thermoelectric response of metallic perovskites: Sr1-xLaxTiO3 (0 ≤ x ≤ 0.1), Phys. Rev. B 63 (11) (2001).

[12] V.C. Coletta, F.C.F. Marcos, F.G.E. Nogueira, M.I.B. Bernardi, A. Michalowicz, R.V. Goncalves, E.M. Assaf, V.R. Mastelaro, In situ study of copper reduction in SrTi1-xCuxO3 nanoparticles, Phys. Chem. Chem. Phys. 18 (3) (2016) 2070–2079.

[13] D. Chen, J.H. Ye, SrSnO3 nanostructures: synthesis, characterization, and photo-catalytic properties, Chem. Mater. 19 (18) (2007) 4585–4591.

[14] Y. Shimizu, M. Shimabukuro, H. Arai, T. Seiyama, Humidity-sensitive character-istics of La3+ doped and undoped SrSnO3, J. Electrochem. Soc. 136 (4) (1989) 1206–1210.

[15] T. Ishihara, H. Fujita, H. Nishiguchi, Y. Takita, SrSnO3-WO3 as capacitive-type nitrogen oxide sensor for monitoring at high temperature, Sens. Actuators B-Chem. 65 (1–3) (2000) 319–324.

[16] Y.F. Li, H.X. Zhang, B.B. Guo, M.D. Wei, Enhanced efficiency dye-sensitized SrSnO3 solar cells prepared using chemical bath deposition, Electrochim. Acta 70 (2012) 313–317.

[17] W.F. Zhang, J.W. Tang, J.H. Ye, Photoluminescence and photocatalytic properties of SrSnO3 perovskite, Chem. Phys. Lett. 418 (1–3) (2006) 174–178.

[18] S. Suzuki, A. Honda, N. Iwaji, S. Higai, A. Ando, H. Takagi, H. Kasatani, K. Deguchi, Ferroelectricity of Sn-doped SrTiO3 perovskites with tin at both A and B sites, Phys. Rev. B 86 (2012).

[19] S. Suzuki, A. Honda, K. Suzuki, S. Higai, A. Ando, K. Niwa, M. Hasegawa, Effects of Sn2+ ion size on Sn doped SrTiO3, Jpn. J. Appl. Phys. 52 (9) (2013).

[20] A.L.M. de Oliveira, M.R.S. Silva, H. Sales, E. Longo, A.S. Maia, A.G. Souza, I.M.G. Santos, Effect of the composition on the thermal behaviour of the SrSn1-xTixO3 precursor prepared by the polymeric precursor method, J. Therm. Anal. Calorim. 114 (2) (2013) 565–572.

[21] Q.Z. Liu, B. Li, H. Li, K. Dai, G.P. Zhu, W. Wang, Y.X. Zhang, G.Y. Gao, J.M. Dai, Composition dependence of structural and optical properties in epitaxial Sr(Sn1-xTix)O3 films, Jpn. J. Appl. Phys. 54 (3) (2015).

[22] T.Q. Wang, K.C. Pitike, Y.K. Yuan, S.M. Nakhmanson, V. Gopalan, B. Jalan, Chemistry, growth kinetics, and epitaxial stabilization of Sn2+ in Sn-doped SrTiO3 using (CH3)(6)Sn-2 tin precursor, Appl. Mater. 4 (12) (2016).

[23] L. Wu, C.C. Wu, M.M. Wu, Humidity sensitivity of Sr(Sn,Ti)O3 ceramics, J. Electron Mater. 19 (2) (1990) 197–200.

[24] S. Sinio, P. Singh, O. Parkash, D. Kumar, Synthesis, microstructure and electrical properties of Ti doped SrSnO3, Adv. Appl. Ceram. 106 (5) (2007) 231–234.

[25] A. Stanulis, A. Selskis, R. Ramanauskas, A. Beganskiene, A. Kareiva, Low temperature synthesis and characterization of strontium stannate-titanate ceramics, Mater. Chem. Phys. 130 (3) (2011) 1246–1250.

[26] T. Nakano, Y. Mikami, K. Abe, S. Suzuki, K. Akiyama, A. Ando, Raman spectroscopic study of ferroelectric Sn-doped $SrTiO_3$, Ferroelectrics 464 (1) (2014) 72–79.

[27] J. Xie, H. Hao, H.X. Liu, Z.H. Yao, Z. Song, L. Zhang, Q. Xu, J.Q. Dai, M.H. Cao, Dielectric relaxation behavior and energy storage properties of Sn modified $SrTiO_3$ based ceramics, Ceram. Int. 42 (11) (2016) 12796–12801.

[28] B.J. Kennedy, I. Qasim, K.S. Knight, Low temperature structural studies of $SrSnO_3$, J. Phys.-Condens. Matter 27 (36) (2015).

[29] A.K. Prodjosantoso, Q.D. Zhou, B.J. Kennedy, Synchrotron X-ray diffraction study of the $Ba_{1-x}SrSnO_3$ solid solution, J. Solid State Chem. 200 (2013) 241–245.

[30] G. Laurita, K. Page, S. Suzuki, R. Seshadri, Average and local structure of the Pb-free ferroelectric perovskites $(Sr,Sn)TiO_3$ and $(Ba,Ca,Sn)TiO_3$, Phys. Rev. B 92 (21) (2015).

[31] D.S. de Melo, M.R.C. Santos, I.M.G. Santos, L.E.B. Soledade, M.I.B. Bernardi, E. Longo, A.G. Souza, Thermal and structural investigation of SnO_2/Sb_2O_3 obtained by the polymeric precursor method, J. Therm. Anal. Calorim. 87 (3) (2007) 697–701.

[32] L.F. da Silva, M.I.B. Bernardi, L.J.Q. Maia, G.J.M. Frigo, V.R. Mastelaro, Synthesis and thermal decomposition of $SrTi_{(1-x)}Fe_xO_3$ $(0.0 \leq x \leq 0.1)$ powders obtained by the polymeric precursor method, J. Therm. Anal. Calorim. 97 (1) (2009) 173–177.

[33] A.M.G. Carvalho, D.H.C. Araujo, H.F. Canova, C.B. Rodella, D.H. Barrett, S.L. Cuffini, R.N. Costa, R.S. Nunes, X-ray powder diffraction at the XRD1 beamline at LNLS, J. Synchrotron Radiat. 23 (2016) 1501–1506.

[34] A.M.G. Carvalho, R.S. Nunes, A.A. Coelho, X-ray powder diffraction of high-absorption materials at the XRD1 beamline off the best conditions: application to (Gd, Nd)(5)Si-4 compounds, Powder Diffr. 32 (1) (2017) 10–14.

[35] B. Ravel, M. Newville, ATHENA, ARTEMIS, HEPHAESTUS: data analysis for X-ray absorption spectroscopy using IFEFFIT, J. Synchrotron Radiat. 12 (2005) 537–541.

[36] B. Ravel, M. Newville, ATHENA and ARTEMIS: interactive graphical data analysis using IFEFFIT, Phys. Scr. T115 (2005) 1007–1010.

[37] V.M. Goldschmidt, Die Gesetze der Krystallochemie, Naturwissenschaften 14 (21) (1926) 477–485.

[38] X.C. Liu, R.Z. Hong, C.S. Tian, Tolerance factor and the stability discussion of ABO_3-type ilmenite, J. Mater. Sci.-Mater. El 20 (4) (2009) 323–327.

[39] R.D. Shannon, Revised effective ionic-radii and systematic studies of interatomic distances in halides and chalcogenides, Acta Crystallogr A 32 (Sep1) (1976) 751–767.

[40] C.J. Ball, B.D. Begg, D.J. Cookson, G.J. Thorogood, E.R. Vance, Structures in the system $CaTiO_3/SrTiO_3$, J. Solid State Chem. 139 (2) (1998) 238–247.

[41] C.J. Howard, H.T. Stokes, Group-theoretical analysis of octahedral tilting in perovskites, Acta Crystallogr. Sect. B-Struct. Sci. 54 (1998) 782–789.

[42] L.Q. Li, B.J. Kennedy, Y. Kubota, K. Kato, R.F. Garrett, Structures and phase transitions in $Sr_{1-x}Ba_xHfO_3$ perovskites, J. Mater. Chem. 14 (2) (2004) 263–273.

[43] D.L. Rousseau, R.P. Bauman, S.P.S. Porto, Normal Mode Determination in Crystals, J. Raman Spectrosc. 10 (1981) 253–290.

[44] B. Mihailova, U. Bismayer, B. Guttler, M. Gospodinov, L. Konstantinov, Local structure and dynamics in relaxor-ferroelectric $PbSc_{1/2}Nb_{1/2}O_3$ and $PbSc_{1/2}Ta_{1/2}O_3$ single crystals, J. Phys.-Condens. Matter 14 (5) (2002) 1091–1105.

[45] M.L. Moreira, E.C. Paris, G.S. do Nascimento, V.M. Longo, J.R. Sambrano, V.R. Mastelaro, M.I.B. Bernardi, J. Andres, J.A. Varela, E. Longo, Structural and optical properties of $CaTiO_3$ perovskite-based materials obtained by microwave-assisted hydrothermal synthesis: an experimental and theoretical insight, Acta Mater. 57 (17) (2009) 5174–5185.

[46] L.F. da Silva, W. Avansi Jr, J. Andres, C. Ribeiro, M.L. Moreira, E. Longo, V.R. Mastelaro, Long-range and short-range structures of cube-like shape $SrTiO_3$ powders: microwave-assisted hydrothermal synthesis and photocatalytic activity, Phys. Chem. Chem. Phys. 15 (29) (2013) 12386–12393.

[47] V.M. Longo, A.T. de Figueiredo, S. de Lazaro, M.F. Gurgel, M.G.S. Costa, C.O. Paiva-Santos, J.A. Varela, E. Longo, V.R. Mastelaro, F.S. De Vicente, A.C. Hernandes, R.W.A. Franco, Structural conditions that leads to photoluminescence emission in $SrTiO_3$: an experimental and theoretical approach, J. Appl. Phys. 104 (2) (2008).

[48] R.V. Vedrinskii, V.L. Kraizman, A.A. Novakovich, P.V. Demekhin, S.V. Urazhdin, Pre-edge fine structure of the 3d atom K x-ray absorption spectra and quantitative atomic structure determinations for ferroelectric perovskite structure crystals, J. Phys.-Condens Matter 10 (42) (1998) 9561–9580.

[49] V.M. Longo, L.S. Cavalcante, R. Erlo, V.R. Mastelaro, A.T. de Figueiredo, J.R. Sambrano, S. de Lazaro, A.Z. Freitas, L. Gomes, N.D. Vieira, J.A. Varela, E. Longo, Strong violet-blue light photoluminescence emission at room temperature in $SrZrO_3$: joint experimental and theoretical study, Acta Mater. 56 (10) (2008) 2191–2202.